Agricultural and Forest Meteorology 279 (2019) 107696

Contents lists available at ScienceDirect

Agricultural and Forest Meteorology

journal homepage: www.elsevier.com/locate/agrformet

Forest wind regimes and their implications on cross-canopy coupling

Anita Freundorfer[a,*], Ingo Rehberg[b], Beverly E. Law[c], Christoph Thomas[a,d]

[a] Micrometeorology, University of Bayreuth, Bayreuth, Germany
[b] Experimental Physics 5, University of Bayreuth, Bayreuth, Germany
[c] Department of Forest Ecosystems & Society, Oregon State University, Corvallis, OR 97331, USA
[d] BayCEER, University of Bayreuth, Bayreuth, Germany

ARTICLE INFO

Keywords:
Weak-wind
Turbulent transport
Decoupling
Subcanopy
Turbulence kinetic energy

ABSTRACT

An analysis of wind regimes across forests of varying density and height is presented. The hockey stick-like dependence of the friction velocity on the mean advective wind speed is used to determine the threshold between the weak-wind and the strong-wind regime for the entire canopy. Such thresholds are compared across four different sites. The height dependence of thresholds within the canopy is inverted compared to the one above grassland sites. This can be understood by extending the accepted interpretation for weak-wind thresholds from grassland sites to forested sites.

Even for large fluctuations above the canopy, the fluctuations of the vertical wind velocity in the subcanopy remain small during weak-wind situations. Correspondingly, in the strong-wind regime, turbulence in the subcanopy remains strong in spite of reduced above-canopy turbulence. This fact suggests that previously used methods for determining the degree of coupling across the canopy layer based upon the ratio of the vertical wind variance between the above-canopy and subcanopy may prove erroneous. Furthermore, it emphasizes the significance of mechanisms generating subcanopy turbulence other than above-canopy turbulent transport and shear.

The transport of mass and energy between the subcanopy and above-canopy layers is significantly reduced during the weak-wind regime. In particular, the vertical turbulent transport is reduced by more than one order of magnitude. This suggests a decoupling of the subcanopy layer during weak-wind situations and allows for the accumulation of carbon dioxide originating from soil respiration in the subcanopy layer during the weak-wind regime.

1. Introduction

The atmospheric boundary layer is a critical part of the earth system where the transfer of momentum is accompanied by the transfer of water vapor, CO_2 and other gases, which is relevant for agriculture, hydrology or pollution. This transfer is driven by turbulence, which thus determines how strongly the earth's surface and the atmosphere are coupled (Van de Wiel et al., 2002; Acevedo et al., 2009; Oliveira et al., 2013).

In a convective boundary layer, there is a clear dependence of the turbulence on stratification. In those situations, the laws governing the turbulent exchange are well understood and represented by the concept of dynamic stability (Monin and Obukhov, 1954; Frisch, 1995). However, several studies show that for weak winds and stable conditions, there is very little dependence of turbulence on stability (Sun et al., 2012; Mahrt et al., 2013; Liang et al., 2014). In particular, there is no critical Richardson number below which turbulence is completely suppressed (Galperin et al., 2007). Instead, turbulence has been observed to increase slowly with increasing wind speed, as long as the wind speed is below a threshold value. For wind speeds higher than that threshold, a more rapid increase of turbulence with wind speed takes place (Sun et al., 2012; Mahrt et al., 2015). While turbulence is driven by the bulk shear in this strong-wind regime, locally generated turbulence and non-stationary motions prevail in the weak-wind regime (Liang et al., 2014). At grassland sites, the air at the height of the sensor is decoupled from the ground during weak-wind situations and coupled to the ground during strong-wind situations (Acevedo et al., 2016). Mahrt et al. (2013) found that the transition wind speed between weak-wind and strong-wind regimes for grassland sites increases with decreasing roughness of the site, while Sun et al. (2012) noted a higher threshold with increasing height.

Although a large fraction of the land surface is covered by forests,

* Corresponding author.
E-mail address: anita.freundorfer@uni-bayreuth.de (A. Freundorfer).

https://doi.org/10.1016/j.agrformet.2019.107696
Received 23 January 2019; Received in revised form 31 July 2019; Accepted 2 August 2019
Available online 26 August 2019
0168-1923/

turbulent exchange within forests is still poorly understood (Villani et al., 2003; Dupont and Patton, 2012). It is more complex compared to the one over short-statured surfaces, since it is strongly influenced by the interaction of the flow with the canopy architecture (Cava and Katul, 2008; Chamecki, 2013). Nevertheless, Russell et al. (2016) showed that it is possible to determine wind regimes in forests with the hockey stick method that Sun et al. (2012) developed originally for the analysis of wind over grasslands.

Within forests, the subcanopy is often poorly coupled to the atmosphere above the canopy, and even within the canopy one can sometimes observe poorly coupled sublayers (Yi, 2009). The subcanopy–canopy decoupling occurs typically in weak-wind situations (Fitzjarrald and Moore, 1990; Oliveira et al., 2013). Unfortunately, this decoupling leads to systematic errors in the flux estimation when using the eddy covariance technique (Aubinet, 2008) for example caused by sporadic mixing events or by cold air drainage (Goulden et al., 1996). This is particularly important for CO_2 fluxes, since forests act as a net sink of CO_2 during the day, but as a net source during the night. With the decoupling mainly occurring during the night, this can lead to a substantial systematic error in the calculation of the net ecosystem exchange (NEE) (Goulden et al., 1996). In order to avoid this miscalculation, particular flux measurement data are often excluded from the analysis, based on a threshold criterion for the friction velocity u_* or the vertical velocity variance σ_w above the canopy (Ruppert et al., 2006; Thomas et al., 2013). While the use of an absolute threshold for u_* has been questioned (Ruppert et al., 2006), Acevedo et al. (2009) found that σ_w is the better indicator since it is less scale dependent than the friction velocity. Van Gorsel et al. (2011) however noted that decoupling can also take place in spite of well-developed turbulence above the canopy.

In order to better understand the turbulent exchange of scalar quantities in forests, the following study will focus on two main objectives:

(1) We use the hockey stick criterion proposed by Sun et al. (2012) for determining an objective threshold for the weak-wind regime. We explore how this threshold is influenced by the canopy by applying the hockey stick approach to multiple locations at 4 different sites with varying vegetation densities. Based on the threshold velocity we find across the profiles of the different forests, we extend the interpretation of Sun et al. (2012) regarding the meaning of the wind speed threshold from grassland sites to forested locations.
(2) We evaluate if there is a connection between the wind regimes determined by hockey stick curves and the coupling of the subcanopy using three different methods for estimating the coupling. With 'decoupled subcanopy' we mean that the transport between the subcanopy and the above canopy is negligibly small, while a significant exchange is taking place when the subcanopy is coupled to the above canopy. For evaluating the coupling, we first use the dependence of the vertical velocity's standard deviation in the subcanopy from the one above the canopy, followed by an analysis of the budget equation of the turbulence kinetic energy. Finally we compare profiles of CO_2 concentrations across the canopy for weak-wind and strong-wind situations.

2. Experimental sites and measure

All the data sets analyzed here were obtained during the Advanced Resolution Canopy FLow Observations (ARCFLO) project. The goal of that project was to study submesoscale processes during weak-wind conditions via an extensive sensor network. A sensor network consists of 8–12 stations, each consisting of one sonic anemometer (Model 81000VRE, R.M. Young, Traverse City, MI) and one thermohygrometer (Vaisala HMP155 and HMP45c, Campbell Scientific, Logan, UT). Such networks, with some varying additional sensors, were deployed at 4 different sites in Oregon, USA, ranging from grassland to heavily forested, and from flat to mountainous. The measurements were all conducted in four field campaigns in consecutive years in late summer during a period of one to two months.

2.1. Botany and Plant Pathology site

The Botany and Plant Pathology (BPP) site is the only unforested study site of the ARCFLO project. It is located in the Willamette river valley near Corvallis, Oregon, USA at 67 m above sea level (44.57° N, 123.24° W). The slightly undulating landscape is used by agriculture and covered by a mix of orchards, hedges and crops of varying height and a few small buildings.

The BPP measurement area lies within a small depression, which is 50 m long, 20 m wide and 1–2 m deep and surrounded by microslopes (see Fig. 1, Zeeman et al. (2015); Mahrt and Thomas (2016)). The plant area index (PAI) in this area is roughly $PAI = 2$. The sensors (8 pairs of sonic anemometers and thermo-hygrometers, and two additional sonic anemometers) were distributed across a 38 m long and 12 m wide measurement area. Most of those were deployed in a height of 1 m above ground level (agl) forming the ground network. Two of the sensor-pairs and the two additional sonic anemometers were mounted on a tower in a height of 1 m, 3 m, 7.5 m and 12 m in order to obtain profile data. Data were taken in the period from August 23 to October 14, 2011 with a sampling frequency of $f = 10$ Hz.

2.2. Metolius Ponderosa Pine site

The Metolius Ponderosa Pine (MP) site is located on the east of the Cascade Mountains (44.451° N, 121.558° W) at an elevation of 1253 m above sea level. It is covered by a sparse ponderosa pine forest and characterized by a very low $PAI = 2.8$. The main canopy extends from 10 m up to a maximum height of $h_c = 16$ m agl (Irvine et al., 2008), but there are also occasional younger and lower trees. The MP site is part of the AmeriFlux Network (US-Me2).

The measurement area is located on a flat saddle where the surrounding topography is very anisotropic (Fig. 1, Vickers et al. (2012)). At the MP site, 12 pairs of sonic anemometers and thermo-hygrometers were mounted across an area of 100 m × 100 m. Four of them were mounted on a tower for profile measurements in a height of $h = 0.125$ m, 5.8 m, 16.75 m and 30.65 m above ground. Another eight formed a grounded network at 1 m agl. Data were taken between June 25 and August 5, 2014 with a sample rate of $f = 20$ Hz. In addition, half-hourly observations of the CO_2 concentrations measured with a LiCor LI 840 (Göckede et al., 2010) are available on a profile across the canopy.

2.3. HJ Andrews Experimental Forest

The third study site is the HJ Andrews Experimental Forest (HJA). The long-term ecological research site is located on the western slope of the cascade mountains in Oregon, USA. The study area is distributed along Watershed 1, an extremely steep basin ranging from 400 m to 900 m above sea level, with slopes up to 40°. The dense canopy consists mainly of Douglas-fir with a dense understory (Daly et al., 2010). The overall PAI varies between $PAI = 2.9$ and $PAI = 10.4$ depending on the location (lower on the slopes, highest at the valley bottom). The canopy height ranges from $h_c = 19$ m at the slopes to $h_c = 28$ m at the valley bottom.

Seven sensor pairs were distributed in a ground network along the valley as well as in a cross-section perpendicular to it. The ground network was set up at 2 m height, due to the dense, up to 1 m tall understory. In addition to that, one sensor pair and two additional sonic anemometers were set up on a tower in a heights of $h = 4$ m, 15.8 m and 38 m. Data were recorded in the period from July 14 to September 17, 2012, with a sample rate of $f = 20$ Hz.

2.4. Mary's River Fir

The Mary's River Fir site (MF) has a plant area index of $PAI = 9.4$ and a canopy height of $h_c = 28$ m. Thus it is most densely vegetated one of the 4 sites. There is an understory with a height up to 0.8 m. Between the understory and the canopy there is a clear bole space. The MF site is located in the coast range of Oregon (44.646° N, 123.551° W) at an elevation of 263 m above sea level. It is surrounded by moderately complex terrain with a gentle saddle in the north-east in a distance of about 600 m (Fig. 1, Thomas (2011)). The MF site is part of the AmeriFlux Network (US-Fir).

The ground network at MF consisted of 4 sensor pairs arranged in a rectangle at 2 m agl, and one sensor pair on the middle of the rectangle. Three additional sensor pairs where mounted on a tower in heights of $h = 14.4$ m, 26.4 m and 28.6 m for obtaining a profile across the canopy. Data were sampled from September 20 to November 2, 2013 with a rate of $f = 20$ Hz. In addition, there is one LiCor LI-7500 gas analyzer in the subcanopy at 4 m agl, which will be used as a supplement to the profile at the MP site.

3. Methods

Turbulent fluctuations are separated from the mean flow using Reynolds decomposition according to

$$u(\mathbf{x}, t) = \bar{u}(\mathbf{x}, t) + u'(\mathbf{x}, t), \tag{1}$$

where u' represents the fluctuating and $\bar{u}$ the mean part of the flow. We use $\tau_p = 1$ min as the perturbation timescale for this separation, except when noted differently. This short timescale is optimized for separating turbulent fluctuations from submeso motions during stable weak-wind situations (Vickers and Mahrt, 2003), where turbulence is only present at very short timescales (Mahrt and Thomas, 2016). We are aware that this short averaging timescale might lead to turbulent motions being included in the mean flow during the day. However, the turbulent fraction will not be contaminated by submesoscale motions which would happen when choosing longer timescales (Vickers and Mahrt, 2006; Mahrt and Thomas, 2016).

In order to separate the weak-wind regime from the strong-wind regime, the dependence of the friction velocity u_* on the mean wind speed $\bar{u}$ is used (Sun et al., 2012). The friction velocity is calculated as

$$u_* = \sqrt[4]{\overline{u'w'}^2 + \overline{v'w'}^2}, \tag{2}$$

u' are the fluctuations of the wind speed in along-wind direction, v' are the ones along the horizontal cross-wind direction, and w' are the ones along the direction orthogonal to u and v (Wilczak et al., 2001). The bin averages of u_* in Fig. 1 exhibit the expected hockey stick-like dependence of the friction velocity on the mean wind speed. The characteristic feature is that they show a slope close to zero for small wind speeds (between $0.1\,\text{m/s} < \bar{u} < 0.5\,\text{m/s}$ in this particular example), and a stronger increase of u_* with $\bar{u}$ for higher wind speeds (Mahrt et al., 2015). The region where u_* is almost independent of $\bar{u}$ is called the weak-wind regime, and the region with the stronger increase of u_* is the strong-wind regime. The threshold u_{thr} between both regimes is determined by fitting a piece-wise linear function to the turbulence data according to

$$u_*(\bar{u}) = \begin{cases} m_1 \cdot \bar{u} + t_1 & \text{if } \bar{u} \le u_{thr}, \\ m_2 \cdot \bar{u} + t_2 & \text{if } \bar{u} > u_{thr}, \end{cases} \tag{3}$$

with $t_2 = (m_1 - m_2) \cdot u_{thr} + t_1$. The threshold u_{thr} is obtained as a fit parameter, along with m_1, m_2, and t_1.

At some stations an additional negative curvature can be seen in the bin averages (Figs. 1 and 2) either for the smallest $\bar{u} < 0.1$ m/s or for the highest $\bar{u}$ of the respective location. A similar behavior was also noted by Mahrt et al. (2015) for the Shallow Cold Pool experiment in Colorado, USA. Since this curvature hinders the detection of the threshold wind speed, those regions are excluded from the fitting algorithm.

In addition to the friction velocity we also use the standard deviation of the vertical wind speed, σ_w, as a measure for the turbulence strength, again using bin averages. This time, a constant number of data points per bin is used in order to get standard errors that are comparable across different bins as opposed to the constant bin width that was used for the hockey stick plots.

The turbulence kinetic energy (TKE) is calculated as

$$\bar{e} = 0.5(\overline{u'^2} + \overline{v'^2} + \overline{w'^2}). \tag{4}$$

Under the assumption of no horizontal transport, the budget of the TKE is

$$\frac{d\bar{e}}{dt} = \frac{g}{\bar{\Theta}_v} \overline{w'\Theta_v'} - \overline{u'w'}\frac{\partial \bar{u}}{\partial z} - \frac{\partial \overline{w'e'}}{\partial z} - \frac{1}{\rho}\frac{\partial \overline{w'p'}}{\partial z} - \epsilon \tag{5}$$

(Foken and Napo, 2008). The temporal development of the TKE is determined by the buoyant production $p_{buoy} = \frac{g}{\bar{\Theta}_v}\overline{w'\Theta_v'}$, the shear production $p_{shear} = \overline{u'w'}\frac{\partial \bar{u}}{\partial z}$, the turbulent transport $t_{turb} = \frac{\partial \overline{w'e'}}{\partial z}$, the pressure transport $t_{pres} = \frac{1}{\rho}\frac{\partial \overline{w'p'}}{\partial z}$ and viscous dissipation ϵ. Θ_v is the virtual potential temperature, g is the earth's acceleration, and z is the height above ground. The air density is ρ, and p' is the pressure fluctuation.

Unlike before, the overbar denotes a 30 minute average for the data evaluation based on Eqs. (4) and (5). A shorter averaging time would lead to missing fluxes that might redistribute turbulence kinetic energy. During weak-wind conditions, this longer averaging time scale will lead to including also fluxes caused by non-turbulent motions. However, for our purpose it is preferable to include all kinds of fluxes that play a role in redistributing TKE or other scalars across the canopy profile. For comparing the TKE budget for the two wind regimes, the differentiation between weak-wind and strong-wind is downsampled. 30-min intervals in which at least 66% of the one minute intervals are classified as weak-wind are assigned to the weak-wind regime and vice versa. Unclear cases, with no dominance of either the weak- or the strong wind regime, are not considered. For differentiating between weak- and strong wind regimes, we always use the ground network sensors at 1–2 m agl and their mean threshold velocity at the respective site.

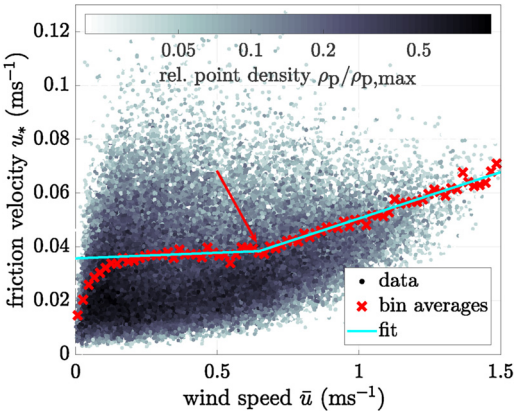

Fig. 1. Detection of the weak-wind threshold for a ground network station in the subcanopy of HJA. Black dots represent the measurement values of $u_*(\bar{u})$, blackness of the points indicates their relative density. The red crosses are bin averages with a constant bin-width of $\Delta\bar{u} = 0.01$ m/s. The blue line is the result of the fit of Eq. (3) to the black points. The arrow points to the threshold u_{thr} determined by the fit. (For interpretation of the references to color in this figure legend, the reader is referred to the web version of this article.)

4. Results and discussion

4.1. What determines the weak-wind threshold?

Comparing the bin-averaged hockey stick curves at four different

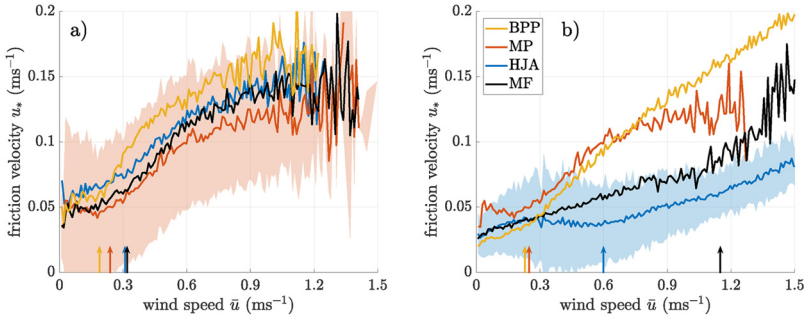

Fig. 2. Dependence of the friction velocity u_* on the mean wind speed $\bar{u}$: (a) at four different sensors of the ground network (1 m height) at the MP site and (b) at one sensor of the ground network of each of the study sites. The colored area shows the standard deviation for one of the sensors and weak-wind thresholds are marked by arrows. (For interpretation of the references to color in this figure legend, the reader is referred to the web version of this article.)

locations of the ground network at the MP site in Fig. 2a, it is evident that for similar terrain the friction velocity shows a similar dependence on the mean wind speed.

The ground network sensors at different sites (Fig. 2b) however exhibit strongly different dependencies of u_* on $\bar{u}$, although all ground network sensors were located at similar heights above the vegetation (the 2 m agl at MF and HJA are due to understory of about 1 m height).

Due to the obvious dependence of the threshold velocity on the site, it is instructive to calculate a site-specific weak-wind threshold. This number is obtained from the average over all the ground network stations within that site, and displayed as a function of the canopy height in Fig. 3.

At the HJA site, there is a large range of canopy heights, since the trees are higher at the valley bottom than on the slopes. Due to that, it is reasonable to split the data into slope stations and valley bottom stations. Among the three forested sites of our study, the site-specific thresholds show a linear increase with the canopy height h_c.

However, the linear relationship does not hold for the BPP site. It is not surprising that results from the ground network sensors at BPP are different from the ones at the other sites of our study, because MF, MP and HJA refer to subcanopy data, while BPP does not. Also the two threshold velocities shown in Fig. 3, which were taken from the literature and describe other unforested sites, do not lie on the line fitted to the data of our forested sites. Clearly, the linear dependence between weak-wind threshold and canopy height that we find for the subcanopy of the forested sites MP, MF, and HJA cannot be extended to grassland sites.

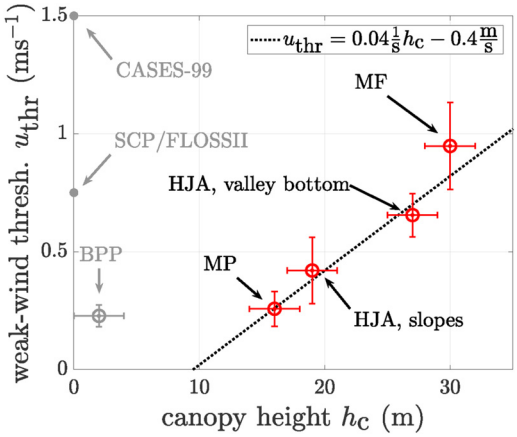

Fig. 3. Site specific weak-wind thresholds in dependence of each site's canopy height. The error bars in u_{thr} direction indicate the standard deviation of the thresholds among all the ground-network sensors of the respective site. BPP is shown in gray since it does not actually have a canopy. In addition, also the thresholds found at the grassland sites SCP and FLOSSII (Mahrt and Thomas, 2016) and CASES-99 (Sun et al., 2012) are shown.

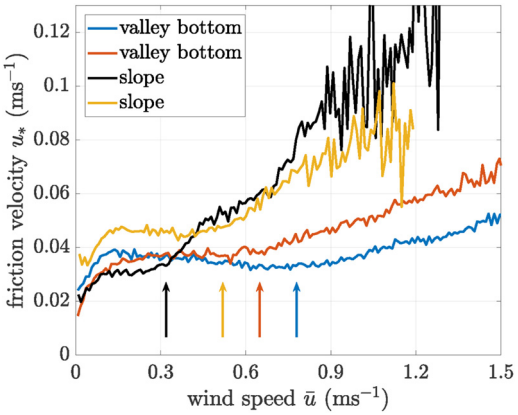

Fig. 4. Bin averaged hockey stick curves for different sensors of the ground network at the HJA site. The weak-wind thresholds are marked by arrows.

Within one site, there can be strong differences between the shapes of the hockey stick curves from different sensors if they have different surrounding micro-topography or micro-scale architecture of the subcanopy. This can be seen most clearly from the sensors at the HJA site (Fig. 4), which is the site with the strongest topographic variations. Ground network stations at the valley bottom generally have a higher weak-wind threshold than the stations at the slopes. Furthermore, the friction velocity measured at the slope stations in the strong-wind regime increases more strongly with increasing wind speed than the one of the valley bottom stations.

Not only the vegetation, but also the sensor height is known to influence the shape of the hockey stick curve. Sun et al. (2012) showed that during the CASES-99 experiment, the threshold between the weak-wind and the strong-wind regime increases logarithmically with height. Our data from the BPP site also show an increase of the threshold wind speed with height, which is not shown in this paper. For the forested sites, however, Fig. 5 displays a different height-dependence.

Within the subcanopy, an increase of the threshold velocity with height cannot be observed at any of the forested sites of our study. At MF, the threshold wind speed decreases towards the top of the canopy from 0.95 m/s at the surface to 0.25 m/s at the canopy top $h_* = \frac{h}{h_c} = 1$. At MP, the threshold wind speed stays relatively constant throughout the subcanopy. Note that the MF site is characterized by a very clear bole space, while the MP site has a subcanopy with significant understory. Above the canopy, the threshold wind speed increases with height as it does above nonforested sites.

There is a difference between subcanopy and grassland sites, which could lead to this different height dependence of the weak-wind threshold. Over grassland sites, TKE develops at the ground and is transported upwards. Sun et al. (2012) and Acevedo et al. (2016) argue that during weak-wind situations classified by the hockey stick

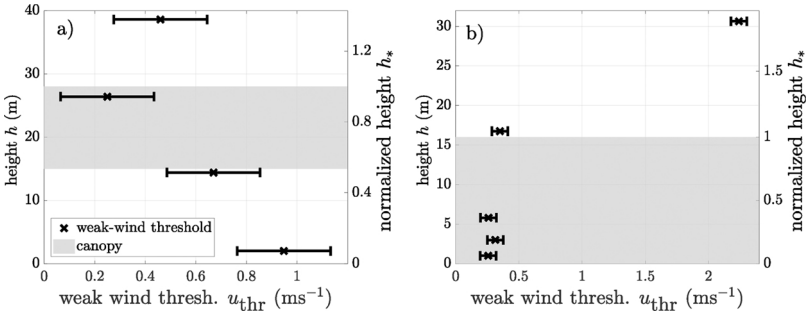

Fig. 5. Profile of the weak wind thresholds found at the MF site (a) and the MP site (b). The extension of the canopy is depicted by a gray background. At MP, there is no clear bole space, which is why also the space below the main canopy is marked in gray.

criterion, the air at the sensor location is decoupled from the ground. This implies that turbulence produced by local shear – and possibly not scaling with local surface roughness and temperature – starts to dominate.

The subcanopy TKE, however, mostly is produced above and within the top of the canopy and is transported downwards (Vickers and Thomas, 2013) (see Fig. 7, discussed in detail in Section 4.2). Consequently, it makes sense that the subcanopy is decoupled from the canopy during a weak-wind situation – in analogy to the decoupling of the air from the ground at grassland sites. This analogy could explain the profile of weak-wind thresholds found for the MF site (Fig. 5a).

The constant and low threshold found at the MP site throughout the subcanopy (Fig. 5b) can be caused by the absence of a clear bole space, as none of the sensors have a big distance from turbulence generating objects. As a result, the sensor locations hardly ever get decoupled from those objects.

The analogy of the weak-wind and strong-wind regimes between forests and grassland sites can also explain the dependence of the weak-wind threshold on the canopy height, since the distance between the subcanopy sensors and the canopy top is bigger for the taller canopies. This allows for a bigger spacing between the ground network sensors and the turbulence generating objects. This also applies for the different thresholds found for valley stations versus slope stations at the HJA site, since the trees on the slopes are shorter than the ones at the valley bottom.

Summarizing these results we can safely conclude that the threshold velocity for the weak-wind regime at a given location is not only determined by the roughness of the surroundings (Mahrt and Thomas, 2016), but also by the distance from the main turbulence generating location.

4.2. Decoupling between subcanopy and above-canopy during weak-wind situations

In order to get a meaningful estimate of the net ecosystem exchange of a forest, it is important to know how the subcanopy is coupled to the above-canopy air. Only if the air communicates across all CO_2 sinks and sources in the vertical, a physically and biologically relevant net CO_2 flux can be calculated. Based on the results in the previous sections, we here evaluate the hypothesis that weak-wind regimes in the subcanopy go along with a decoupling of the subcanopy from the above-canopy atmosphere.

As an indicator for such a decoupling, we plot the standard deviation of the vertical velocity component of a subcanopy sensor $\sigma_{w,s}$ in dependence on that of an above-canopy sensor $\sigma_{w,a}$ in Fig. 6. According to Thomas et al. (2013), the case where the turbulence in the subcanopy is independent from that above the canopy – i.e., $\sigma_{w,s}(\sigma_{w,a})$ has a slope close to zero – is a hallmark for decoupling. In contrast, coupling is manifested by a monotonic increase of $\sigma_{w,s}$ with $\sigma_{w,a}$. Fig. 6 illustrates the fact that for none of the evaluated forested sites a striking difference in the slopes of the $\sigma_{w,a}$-$\sigma_{w,s}$ plots between weak-wind and strong-wind cases can be seen. On the contrary, the slope is fairly similar between weak-wind and strong-wind regimes.

The most striking feature of Fig. 6 is the offset between the weak-wind and the strong-wind data. It shows that the subcanopy turbulence is generally much higher in the strong-wind than in the weak-wind regime. Even for a high above canopy $\sigma_{w,a}$, weak-wind regime intervals show a lower subcanopy $\sigma_{w,s}$ than those strong-wind intervals with a relatively small $\sigma_{w,a}$. Precisely speaking, at the MF site, 92% of the weak-wind intervals have a lower subcanopy turbulence than any of the strong wind intervals. The slope in the dependence between the subcanopy and above canopy σ_w however is very similar between weak-wind and strong-wind (Fig. 6, dashed/dotted lines).

Also at MP (Fig. 6b), for around 97% of the data, weak-wind and strong-wind regime exhibit very similar slopes, but a clear offset. Only strong-wind cases with very low above-canopy turbulence $\sigma_{w,a} \lesssim 0.2$ m/s show a deviating slope. Those cases correspond to data that has been classified as strong wind data by the wind speed threshold criterion but occurs during a time with frequent switches between the weak-wind and strong-wind regime or at the beginning or end of a weak-wind interval.

We conclude from the analysis of Fig. 6 that a characteristic difference of the $\sigma_{w,s}(\sigma_{w,a})$-slopes between weak- and strong-wind regimes cannot be observed. However, the strongly reduced subcanopy turbulence in the weak-wind regime does suggest that decoupling may occur during weak-wind situations.

To elucidate the connection between coupling and subcanopy turbulence, we examine the TKE budget across the canopy as a second indicator for the amount of coupling. Fig. 7a shows profiles of relative budget terms $\lambda_x = \frac{d\bar{e}_x}{dt}/\bar{e}$. The index x refers to different parts at the rhs of Eq. (5), and $\bar{e}$ the TKE of the respective layer and wind regime, done separately for the weak-wind and strong-wind conditions determined by the hockey stick method.

The shapes of the four λ_x profiles show some similarity during weak-wind and strong-wind conditions. Note that these terms have been divided by the TKE of the respective layer and wind regime. The magnitude of the absolute TKE terms is reduced during weak-wind. For all three layers, the overall TKE is an order of magnitude higher during strong-wind conditions. For instance, the average TKE in the subcanopy layer is $\bar{e}_{sub} = 0.013\,m^2/s^2$ in the weak-wind regime and $\bar{e}_{sub} = 0.17\,m^2/s^2$ during strong-wind conditions.

The most obvious difference between weak-wind and strong-wind regime can be found in the buoyancy term of the TKE budget (Fig. 7b), where the absolute values are similar but the sign is flipped during weak-wind compared to the strong-wind regime. This indicates that the weak-wind and strong-wind regimes are closely correlated with an inversion of the thermal gradient, with the weak-wind regime occurring most often during stable conditions. As a result, buoyancy is mainly a source of TKE during strong wind and a sink of TKE during weak winds.

While the magnitude of almost all TKE budget terms is reduced during the weak-wind regime, the turbulent transport term λ_{turb} is suppressed most strongly. During strong-wind conditions, the turbulent

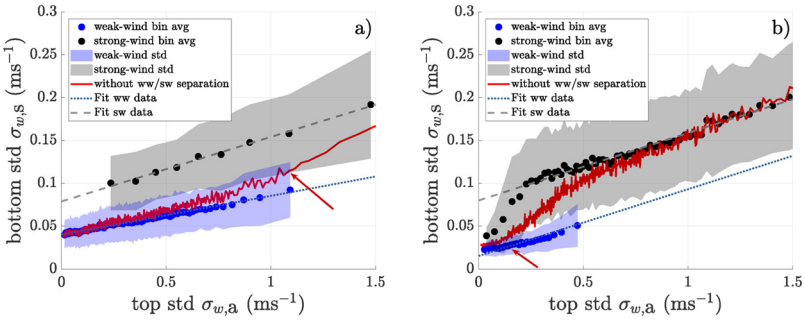

Fig. 6. Dependence of the subcanopy vertical wind standard deviation $\sigma_{w,s}$ on the above-canopy one ($\sigma_{w,a}$) at (a) the MF site and (b) the MP site. Black dots represent bin-averaged values for the strong wind regime and blue dots for the weak-wind regime. Each dot represents an average of 500 observations. The red line corresponds to the bin averages without a separation for the wind regimes and the red arrow marks the point where the slope of the red line (weak-wind and strong-wind cases combined) shows a sudden increase. The dashed and dotted lines show a fit of a linear function to the weak- and strong-wind data respectively, whereby strong wind data with $\sigma_{w,a} < 0.2$ m/s were excluded for MP. (For interpretation of the references to color in this figure legend, the reader is referred to the web version of this article.)

transport is the second largest term if the TKE budget and only exceeded by the residual (which contains advection, pressure transport, viscous dissipation and any measurement error). In particular, it is the strongest source of TKE in the subcanopy during strong wind conditions. During weak-wind conditions, however, the turbulent transport term is almost zero at all levels across the canopy (Fig. 7c). In the subcanopy, the turbulent transport is smaller than all the other TKE budget terms analysed. The strongly suppressed turbulent transport during weak-wind situations suggests a concomitant decoupling between subcanopy and above-canopy during weak-wind situations.

Thirdly, the positive sign of the residual term λ_{res} in the weak-wind subcanopy suggests a possible systematic error in measurements of ecosystem respiration during weak-wind situations. Along with the loss of TKE due to viscous dissipation and the pressure transport, the residual term also contains the horizontal advection. The viscous dissipation always is a sink of TKE. Using the same data set at the MP site, Ehrnsperger (2017) found that the pressure transport is small compared to the other TKE budget terms. While there is a large spread in the subcanopy residual, in 73% of the cases, the residual is positive during weak-wind situations. The positive sign of the residual term suggests that advection gains a big influence during weak-wind conditions, often even outweighing the destruction of TKE by viscous dissipation (Ehrnsperger, 2017). With strong advection, flux measurements taken above the forest cannot represent the true ecosystem respiration (Staebler and Fitzjarrald, 2004).

Both, the $\sigma_{w,a}$–$\sigma_{w,s}$ plot (Fig. 6) and the TKE budget profiles (Fig. 7) revealed that the vertical turbulent transport is strongly reduced during weak-wind conditions. This might explain that the CO_2 profiles from the MP site (Fig. 8) reveal a noticeable accumulation of CO_2 within the subcanopy. There is almost no overlap between the typical CO_2 concentrations of weak-wind and strong-wind situations. For the MF site, the gas analyzer in the subcanopy also shows higher CO_2 concentrations in the weak-wind case than during strong wind, as indicated by the square and circle in Fig. 8. All in all, the subcanopy seems to be mostly decoupled from the above canopy during weak-wind indications due to the strongly reduced vertical turbulent transport.

4.3. Using $\sigma_{w,a}$ as decoupling indicator

When investigating the dependence of the standard deviation of the

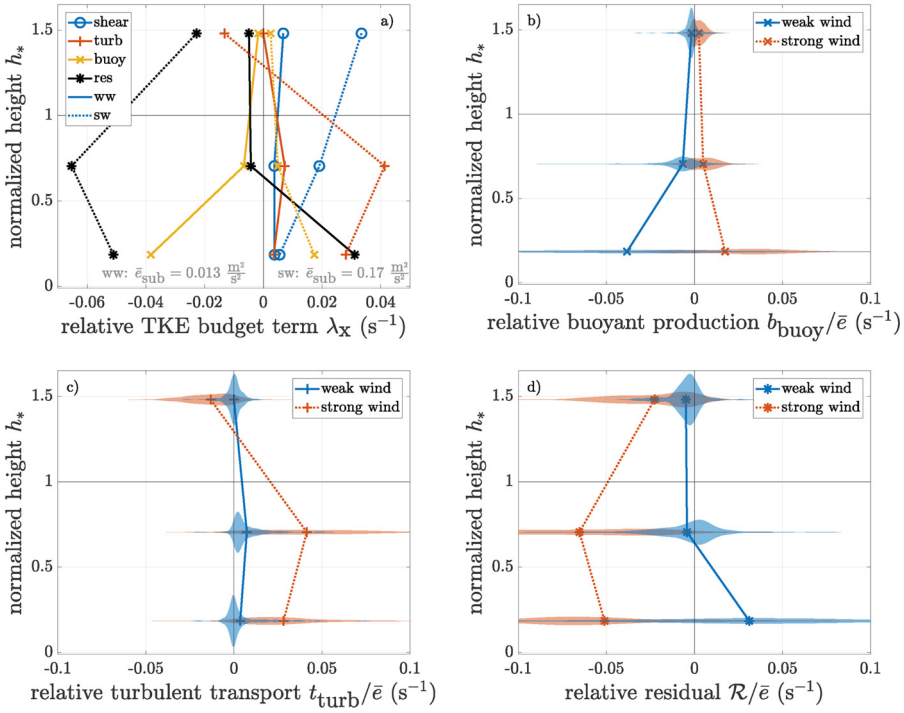

Fig. 7. (a) Profiles of relative TKE budget terms along the tower at the MP site. Solid lines represent the TKE budget terms during weak-wind (ww) situations, dotted lines refer to strong-wind situations (sw). The gray numbers at the bottom indicate the average TKE in the subcanopy during weak-wind and strong-wind conditions, respectively. (b)–(d) Probability distributions of relative buoyant production, turbulent transport and residual for weak-wind and strong-wind regime at the respective heights derived by a kernel density estimation. (For interpretation of the references to color in this figure legend, the reader is referred to the web version of this article.)

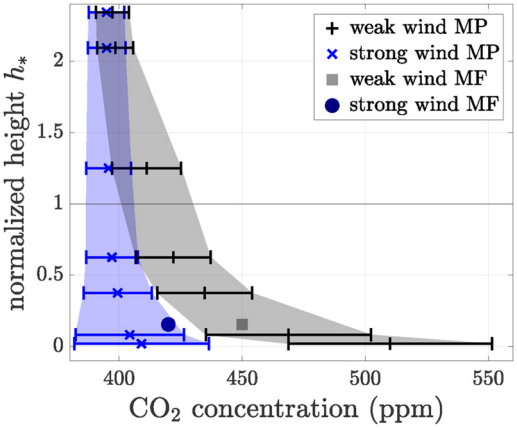

Fig. 8. Profiles of the average molar CO_2 concentrations at MP separated for weak-wind (black +) and strong-wind conditions (blue crosses). Error bars and shaded areas mark the region within one standard deviation around the average. In addition, the average weak-wind (gray square) and strong-wind (blue circle) concentration in the subcanopy of MF are shown. (For interpretation of the references to color in this figure legend, the reader is referred to the web version of this article.)

vertical wind component in the subcanopy $\sigma_{w,s}$ from the one above the canopy $\sigma_{w,a}$ (Fig. 6), the weak-wind data and the strong-wind data show an almost identical slope. On the basis of earlier findings (Thomas et al., 2013), a higher slope for the strong-wind situation than for the weak-wind one could have been expected, since the subcanopy is largely decoupled in the weak-wind regime,

If one looks at the dependence of $\sigma_{w,s}$ on $\sigma_{w,a}$ without the separation for weak-wind and strong wind, there actually is a transition from a lower to a higher slope (marked by an arrow in Fig. 6). However, this should not be considered as a direct indication for a stronger coupling: When comparing this combined $\sigma_{w,s}(\sigma_{w,a})$ behavior to the separated weak-wind and strong-wind ones, this change of the slope seems to be caused by strong-wind cases starting to outweigh weak-wind cases for higher above-canopy turbulence.

Instead of $\sigma_{w,a}$, the subcanopy wind regime seems to have the dominating influence on the vertical transport in the subcanopy. Almost all weak-wind cases show a lower $\sigma_{w,s}$ than the strong wind cases, even for strong above canopy turbulence $\sigma_{w,a}$. This observation agrees well with the findings of Van Gorsel et al. (2011). They showed that the bole space can be decoupled and have a strong stable stratification, even for fully developed turbulence above the canopy. The turbulence – and consequently also the turbulent transport – in the subcanopy is more strongly determined by the subcanopy wind regime than by the turbulence strength above the canopy.

5. Conclusion

The dependence of the friction velocity on the mean wind speed yields an objective measure to distinguish between weak and strong wind via the hockey stick criterion. Applying this method to a variety of locations within four different sites with varying forest density reveals the highest threshold wind speeds u_{thr} at the tallest, most densely forested site, which is also characterized by a very clear bole space. The lowest thresholds are found at a grassland site, closely followed by a short, open forest.

Within a site, there is a height dependence of the threshold. In contrast to grassland sites, where the threshold increases with increasing height, in forested sites the threshold decreases towards the canopy top. This can be understood by extending the interpretation of Sun et al. (2012) from grassland sites to forested sites: In both cases the weak-wind threshold increases with increasing distance from those roughness elements which are the main generator of a location's TKE. During weak-wind situations, the measuring location is largely decoupled from these TKE-generators.

We find that the vertical turbulent transport is close to zero for wind speeds lower than the weak-wind threshold compared to higher wind speeds. The other TKE terms are reduced as well, but the effect is particularly strong for the turbulent transport. The accumulation of CO_2 in the subcanopy during weak-wind situations can be understood as a result of this strongly reduced vertical transport.

During the weak-wind regime, advection plays an enhanced role within the TKE budget and CO_2 accumulates in the subcanopy due to limited vertical transport. This indicates that measurements of the forest's respiration rate taken with eddy covariance systems above the canopy during those periods will likely underestimate its true CO_2 budget. Part of the carbon that is accumulated during the weak-wind situations will be emitted during consecutive strong-wind periods and thus compensate for the preceding underestimation. However any advection taking place during weak-wind periods when a carbon is accumulated in the subcanopy will lead to a miscalculation of the CO_2 budget.

Finally we like to stress that the bend in $\sigma_{w,s}(\sigma_{w,a})$-plots, which has frequently been used as a decoupling indicator for avoiding the underestimation of the CO_2 flux, may be caused by the concurrence of the strong-wind regime at high $\sigma_{w,a}$ above the canopy and the weak-wind regime at low $\sigma_{w,a}$. The vertical wind speed fluctuations in the subcanopy are generally lower in the weak-wind regime than in the strong-wind regime, independent of the above-canopy fluctuations. Because the subcanopy turbulent transport is much more dependent on the subcanopy wind regime than on the turbulence strength above canopy, it is questionable, whether the $\sigma_{w,a}$–$\sigma_{w,s}$ plot is a reliable method for estimating the coupling. Since decoupling can happen in spite of considerable turbulence above the canopy, it seems crucial to have a sensor in the subcanopy in order to estimate the amount of coupling between the subcanopy and the above-canopy layers. Future studies should explicitly test, whether subcanopy sensors can improve the filtering and thus our estimates of CO_2 fluxes across the canopy and compare it with existing methods like the u_* filtering or the σ_w filtering done with an above canopy sensor. This could include testing the wind regime method in a more homogeneous terrain, since none of the presented sites offer ideal conditions for the eddy covariance method due to the heterogeneous surrounding topography.

Acknowledgements

This research was supported by the U.S. Department of Energy (DOE), Office of Science (BER), contract DE-FG02-06ER64318, and the National Science Foundation, Physical & Dynamic Meteorology, award AGS 0955444. Research was conducted at HJ Andrews Experimental Forest, which is funded by the US Forest Service, Pacific Northwest Research Station.

References

Acevedo, O.C., Mahrt, L., Puhales, F.S., Costa, F.D., Medeiros, L.E., Degrazia, G.A., 2016. Contrasting structures between the decoupled and coupled states of the stable boundary layer. Q. J. R. Meteorol. Soc. 142 (695), 693–702.

Acevedo, O.C., Moraes, O.L., Degrazia, G.A., Fitzjarrald, D.R., Manzi, A.O., Campos, J.G., 2009. Is friction velocity the most appropriate scale for correcting nocturnal carbon dioxide fluxes? Agric. Forest Meteorol. 149 (1), 1–10.

Aubinet, M., 2008. Eddy covariance CO_2 flux measurements in nocturnal conditions: an analysis of the problem. Ecol. Appl. 18 (6), 1368–1378.

Cava, D., Katul, G.G., 2008. Spectral short-circuiting and wake production within the canopy trunk space of an alpine hardwood forest. Bound.-Layer Meteorol. 126 (3), 415–431.

Chamecki, M., 2013. Persistence of velocity fluctuations in non-Gaussian turbulence within and above plant canopies. Phys. Fluids 25 (11), 115110.

Daly, C., Conklin, D.R., Unsworth, M.H., 2010. Local atmospheric decoupling in complex topography alters climate change impacts. Int. J. Climatol. 30 (12), 1857–1864.

Dupont, S., Patton, E.G., 2012. Influence of stability and seasonal canopy changes on micrometeorology within and above an orchard canopy: the chats experiment. Agric. Forest Meteorol. 157, 11–29.

Ehrnsperger, L., 2017. Experimental Evaluation of the Significance of the Pressure Transport Term to the Turbulence Kinetic Energy Budget Across Contrasting Forest Architectures (Master's thesis). University of Bayreuth, Bayreuth, Germany (Last accessed 19.10.18). http://www.bayceer.uni-bayreuth.de/meteo/de/top/diss/14/143109/MA_TKE_LE.pdf.

Fitzjarrald, D.R., Moore, K.E., 1990. Mechanisms of nocturnal exchange between the rain forest and the atmosphere. J. Geophys. Res.: Atmos. 95 (D10), 16839–16850.

Foken, T., Napo, C.J., 2008. Micrometeorology, vol. 2 Springer.

Frisch, U., 1995. Turbulence: The Legacy of A. N. Cambridge University Press, Kolmogorov.

Galperin, B., Sukoriansky, S., Anderson, P.S., 2007. On the critical Richardson number in stably stratified turbulence. Atmos. Sci. Lett. 8 (3), 65–69.

Göckede, M., Michalak, A.M., Vickers, D., Turner, D.P., Law, B.E., 2010. Atmospheric inverse modeling to constrain regional-scale CO_2 budgets at high spatial and temporal resolution. J. Geophys. Res.: Atmos. 115 (D15).

Goulden, M.L., Munger, J.W., Fan, S.-M., Daube, B.C., Wofsy, S.C., 1996. Measurements of carbon sequestration by long-term eddy covariance: methods and a critical evaluation of accuracy. Glob. Change Biol. 2 (3), 169–182.

Irvine, J., Law, B., Martin, J., Vickers, D., 2008. Interannual variation in soil CO_2 efflux and the response of root respiration to climate and canopy gas exchange in mature ponderosa pine. Glob. Change Biol. 14 (12), 2848–2859.

Liang, J., Zhang, L., Wang, Y., Cao, X., Zhang, Q., Wang, H., Zhang, B., 2014. Turbulence regimes and the validity of similarity theory in the stable boundary layer over complex terrain of the Loess Plateau, China. J. Geophys. Res.: Atmos. 119 (10), 6009–6021.

Mahrt, L., Sun, J., Stauffer, D., 2015. Dependence of turbulent velocities on wind speed and stratification. Bound.-Layer Meteorol. 155 (1), 55–71.

Mahrt, L., Thomas, C., Richardson, S., Seaman, N., Stauffer, D., Zeeman, M., 2013. Non-stationary generation of weak turbulence for very stable and weak-wind conditions. Bound.-Layer Meteorol. 147 (2), 179–199.

Mahrt, L., Thomas, C.K., 2016. Surface stress with non-stationary weak winds and stable stratification. Bound.-Layer Meteorol. 159 (1), 3–21.

Monin, A., Obukhov, A., 1954. Basic laws of turbulent mixing in the surface layer of the atmosphere. Contrib. Geophys. Inst. Acad. Sci. USSR 151 (163), e187.

Oliveira, P.E., Acevedo, O.C., Moraes, O.L., Zimermann, H.R., Teichrieb, C., 2013. Nocturnal intermittent coupling between the interior of a pine forest and the air above it. Bound.-Layer Meteorol. 146 (1), 45–64.

Ruppert, J., Mauder, M., Thomas, C., Lüers, J., 2006. Innovative gap-filling strategy for annual sums of CO_2 net ecosystem exchange. Agric. Forest Meteorol. 138 (1–4), 5–18.

Russell, E.S., Liu, H., Gao, Z., Lamb, B., Wagenbrenner, N., 2016. Turbulence dependence on winds and stability in a weak-wind canopy sublayer over complex terrain. J. Geophys. Res.: Atmos. 121 (19).

Staebler, R.M., Fitzjarrald, D.R., 2004. Observing subcanopy CO_2 advection. Agric. Forest Meteorol. 122 (3–4), 139–156.

Sun, J., Mahrt, L., Banta, R.M., Pichugina, Y.L., 2012. Turbulence regimes and turbulence intermittency in the stable boundary layer during cases-99. J. Atmos. Sci. 69 (1), 338–351.

Thomas, C.K., 2011. Variability of sub-canopy flow, temperature, and horizontal advection in moderately complex terrain. Bound.-Layer Meteorol. 139 (1), 61–81.

Thomas, C.K., Martin, J.G., Law, B.E., Davis, K., 2013. Toward biologically meaningful net carbon exchange estimates for tall, dense canopies: multi-level eddy covariance observations and canopy coupling regimes in a mature Douglas-fir forest in Oregon. Agric. Forest Meteorol. 173, 14–27.

Van de Wiel, B., Ronda, R., Moene, A., De Bruin, H., Holtslag, A., 2002. Intermittent turbulence and oscillations in the stable boundary layer over land. Part I: a bulk model. J. Atmos. Sci. 59 (5), 942–958.

Van Gorsel, E., Harman, I.N., Finnigan, J.J., Leuning, R., 2011. Decoupling of air flow above and in plant canopies and gravity waves affect micrometeorological estimates of net scalar exchange. Agric. Forest Meteorol. 151 (7), 927–933.

Vickers, D., Irvine, J., Martin, J.G., Law, B.E., 2012. Nocturnal subcanopy flow regimes and missing carbon dioxide. Agric. Forest Meteorol. 152, 101–108.

Vickers, D., Mahrt, L., 2003. The cospectral gap and turbulent flux calculations. J. Atmos. Oceanic Technol. 20 (5), 660–672.

Vickers, D., Mahrt, L., 2006. A solution for flux contamination by mesoscale motions with very weak turbulence. Bound.-Layer Meteorol. 118 (3), 431–447.

Vickers, D., Thomas, C.K., 2013. Some aspects of the turbulence kinetic energy and fluxes above and beneath a tall open pine forest canopy. Agric. Forest Meteorol. 181, 143–151.

Villani, M., Schmid, H.P., Su, H.-B., Hutton, J., Vogel, C.S., 2003. Turbulence statistics measurements in a northern hardwood forest. Bound.-Layer Meteorol. 108 (3), 343–364.

Wilczak, J.M., Oncley, S.P., Stage, S.A., 2001. Sonic anemometer tilt correction algorithms. Bound.-Layer Meteorol. 99 (1), 127–150.

Yi, C., 2009. Instability analysis of terrain-induced canopy flows. J. Atmos. Sci. 66 (7), 2134–2142.

Zeeman, M.J., Selker, J.S., Thomas, C.K., 2015. Near-surface motion in the nocturnal, stable boundary layer observed with fibre-optic distributed temperature sensing. Bound.-Layer Meteorol. 154 (2), 189–205.